3D characterization of porosity and minerals of low-permeability uranium-bearing sandstone based on multi-resolution image fusion

Bing Sun[1] · Shan-Shan Hou[1] · Sheng Zeng[2] · Xin Bai[2] · Shu-Wen Zhang[2] · Jing Zhang[3]

Abstract In the process of in situ leaching of uranium, the microstructure controls and influences the flow distribution, percolation characteristics, and reaction mechanism of lixivium in the pores of reservoir rocks and directly affects the leaching of useful components. In this study, the pore throat, pore size distribution, and mineral composition of low-permeability uranium-bearing sandstone were quantitatively analyzed by high pressure mercury injection, nuclear magnetic resonance, X-ray diffraction, and wavelength-dispersive X-ray fluorescence. The distribution characteristics of pores and minerals in the samples were qualitatively analyzed using energy-dispersive scanning electron microscopy and multi-resolution CT images. Image registration with the landmarks algorithm provided by FEI Avizo was used to accurately match the CT images with different resolutions. The multi-scale and multi-mineral digital core model of low-permeability uranium-bearing sandstone is reconstructed through pore segmentation and mineral segmentation of fusion core scanning images. The results show that the pore structure of low-permeability uranium-bearing sandstone is complex and has multi-scale and multi-crossing characteristics. The intergranular pores determine the main seepage channel in the pore space, and the secondary pores have poor connectivity with other pores. Pyrite and coffinite are isolated from the connected pores and surrounded by a large number of clay minerals and ankerite cements, which increases the difficulty of uranium leaching. Clays and a large amount of ankerite cement are filled in the primary and secondary pores and pore throats of the low-permeability uranium-bearing sandstone, which significantly reduces the porosity of the movable fluid and results in low overall permeability of the cores. The multi-scale and multi-mineral digital core proposed in this study provides a basis for characterizing macroscopic and microscopic pore-throat structures and mineral distributions of low-permeability uranium-bearing sandstone and can better understand the seepage characteristics.

Keywords Low-permeability uranium-bearing sandstone · Digital core · Micro-CT · SEM–EDS · Image fusion

✉ Sheng Zeng
  usczengs@126.com

1   School of Civil Engineering, University of South China, Hengyang 421001, China

2   School of Resource Environment and Safety Engineering, University of South China, Hengyang 421001, China

3   School of Resources and Safety Engineering, Central South University, Changsha 410083, China

1 Introduction

The in situ leaching process of sandstone uranium ore can be regarded as the flow process of lixivium in the connected pores of reservoir rocks. The uranium stored in the rock minerals is dissolved into the lixivium under the action of a chemical solution and then migrates out from the surface of the rock pores with the leachate [1, 2]. The mineral components in uranium-bearing sandstones provide the material basis for pore formation and evolution and directly control the quality of reservoirs [3, 4]. The microstructure of uranium ore rocks and the connectivity of

pores have an important impact on lixivium transport. Microscopic study of the mineral and pore distribution characteristics of uranium-bearing sandstone is of great significance. A large number of successful studies of microstructure of reservoir rocks have been performed worldwide. The research methods can be summarized into three categories: experimental data analysis technology, image analysis technology, and digital core technology [5].

The experimental data analysis techniques for the microscopic pore structure of reservoir rock mainly include high pressure mercury injection (HPMI), constant-speed mercury injection (CRMI), nuclear magnetic resonance (NMR), gas adsorption, and neutron small angle scattering (SANS) experiments. The throat size of a certain level of rock and the distribution of the pore throat volume controlled by the corresponding throat can be obtained through the HPMI experiment, which is the main method to measure the capillary pressure of rocks. However, due to the limitation of mercury injection pressure, it cannot fully reflect the reservoir pore space [6, 7]. NMR transforms the T_2 spectrum of nuclear magnetic resonance into the distribution curve of pore radius, which can be used to evaluate the pore structure of cores and characterize the pore size distribution at multi-scales, but it cannot obtain the seepage capacity of reservoir rocks [8, 9]. X-ray diffraction (XRD) and X-ray fluorescence (XRF) tests are conventional quantitative analysis methods for minerals in geological research [10, 11]. However, these methods cannot analyze the morphology characteristics of minerals and only quantitatively analyze their content.

Image analysis techniques collect images of core sections through high-resolution instruments and facilitate qualitative analysis of the mineral morphology, and pore and throat size distribution and connectivity in rocks. The image analysis techniques of reservoir rock microstructure include cast thin sections, scanning electron microscopy (SEM), micro/nano-CT scanning, and focused ion beam SEM (FIB-SEM). As a low-cost two-dimensional (2D) imaging technology with high resolution that can detect nanopores, SEM is widely used in the analysis of microscopic pore structure and mineral characteristics of reservoir rocks [12, 13]. The SEM images combined with energy spectrometer, elemental scanning analyzer, and cathode luminescence measurements can identify mineral types and generate mineral distribution diagrams. By means of energy-dispersive scanning electron microscopy (EDS–SEM), the morphological characteristics, pore types, genesis, output, and occurrence of various minerals on the microscopic scale can be studied [14–16]. Compared with the cast thin sections and SEM, micro/nano-CT scanning has the advantages of nondestructive measurement, intuitive measurement results, and accurate description of spatial characteristics of microstructure, which is widely

used in the construction of various rock digital cores and pore network models [17–19]. FIB-SEM can observe the distribution and connectivity of nanopores of unconventional tight rocks such as natural gas shale and fine sandstone more clearly. However, it is not widely used owing to the high cost of sample preparation and limited scope of observation [20, 21].

Digital core technologies obtain the microstructure characteristics of rocks without destroying the real cores by using various microimaging techniques. On this basis, various algorithms are used to construct three-dimensional (3D) digital core models of rocks [22, 23]. The combination of the reconstructed digital core and multi-field coupling finite element technologies is used widely for fluid seepage simulation of rock–fluid systems, which can realize data visualization at the pore level and deepen the understanding of various flow mechanisms [24–29]. Digital petrophysics experiments can not only be verified by laboratory experiments, but can also explain petrophysics and chemistry experiments from a microscopic perspective, which can replace laboratory experiments when appropriate samples cannot be obtained [30–32]. Numerical simulation of petrophysics based on digital core technologies has become an important means of petrophysics research. However, the core size is small and the representative volume cannot be obtained when the resolution of the micro-CT scan is high. In addition, micro-CT scanning has the disadvantage of not characterizing the mineral composition information, which is very important for physicochemical seepage simulation of reservoir rocks [33]. Therefore, it is necessary to describe the core structure using several methods.

Image fusion refers to the process in which images of the same scene obtained by different instruments or the same scene obtained by the same instrument at different times are de-noised, time registered, spatially registered, or resampled by some mathematical algorithm to obtain a higher quality synthetic image [34, 35]. It can overcome the existence of single sensor image in geometry, spectrum, and spatial resolution limitations and differences. Multiresolution image fusion for reservoir microstructure analysis is currently a hot research topic [18]. For example, Markussen et al. [36] analyzed the pore distribution and the connectivity between pore and throat by using dry/wet difference mapping CT scan method and discussed the influence of carbonate cementation on porosity and porethroat characteristics. According to the registration of 2D-to-3D images, the nanoscale data in 2D slices can be directly related to the microscale features in 3D images [37, 38]. Combining micro-CT with SEM images can improve information on microporosity and microstructure of analyzed samples, and the mineral information in CT image can be recognized to allow the visualization of

spatial distribution of different mineral phases based on automated mineralogy mapping by SEM–EDS [14]. Liu et al. [39] established multi-mineral digital core of tight sandstone by using SEM–EDS combined with CT images and analyzed different pore types and their connectivity in tight sandstone by using expansion algorithm. Based on the superposition method, Lin et al. [40] reconstructed the double pore 3D digital cores of carbonate rocks by using micro-CT combined with SEM images and analyzed its seepage characteristics by lattice Boltzmann method.

The low permeability of uranium ores is one of the key factors restricting the successful production of in situ leaching of sandstone-type uranium deposits. Low-permeability uranium-bearing sandstone forms different pore types under geological and sedimentary processes, and the pore structure is complex [41, 42]. At the same time, its internal mineral composition changes greatly, while different mineral compositions and structures have different physicochemical properties, which have an important influence on the seepage of lixivium [43]. At present, studies on in situ leaching solute transport in uranium ore are rarely carried out from a microperspective [44]. In this study, the microstructure characteristics of low-permeability uranium-bearing sandstone were studied using comprehensive testing methods. The low-permeability uranium-bearing sandstone cores were scanned by medium- and high-resolution micro-CT, and the core surface was tested by EDS–SEM. The feature-based image registration method is used to accurately match CT images with different resolutions in the Avizo software. The low-permeability uranium-bearing digital core model was established after pore segmentation and mineral segmentation on fusion CT images by K-means clustering segmentation and the watershed segmentation method combined with EDS–SEM images. It is expected to provide a deep understanding of the microstructural characteristics of low-permeability uranium-bearing sandstone and provide a model basis for the subsequent study of the influence of pore structure and mineral distribution on the seepage characteristics of lixivium.

2 Samples and experimental methods

2.1 Sample source and collection

The Monchgur uranium deposit is from the interlayer oxidation zone of the Middle–lower Jurassic Shuixigou group zone sandstone-type rolled uranium deposit located in the southern margin of the Yili Basin, Xinjiang, China. The hydraulic conductivity of the entire ore-bearing aquifer is less than 0.5 m/d, which belongs to the low-permeability ore body type. The uranium deposit has a special structure and hydrodynamic conditions. At the same time, the sand bodies of the Sangonghe Formation are the best developed in the southern margin of the Yili Basin with good lithofacies and lithologic conditions, which is conducive to the infiltration of oxidation fluid and the formation of uranium ore bodies [2]. Therefore, two representative sandstone samples from the upper member of the Sangonghe Formation are selected in this study. The selected samples belong to gray medium sandstone, which is mainly
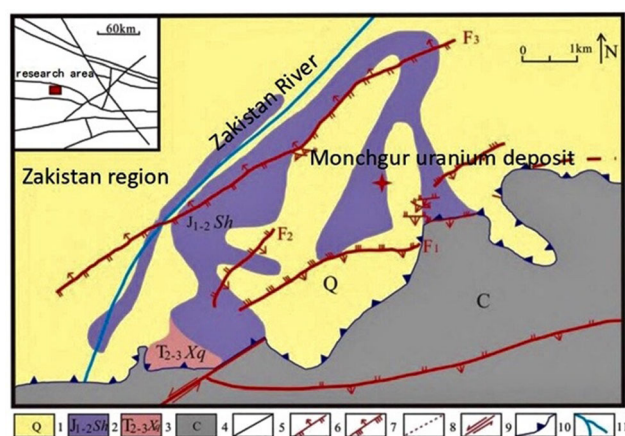

Fig. 1 (Color online) Geological Sketch map of Monchgur region [45]. (1) Quaternary loose deposits; (2) Middle–lower Jurassic Shuixigou group gray conglomerate, sandstone and siltstone; (3) Middle–upper Triassic Xiaoqungou group gray and variegated glutenite and mudstone; (4) carboniferous moderate-acidic volcanic rocks; (5) regional fault; (6) overfault; (7) thrust fault; (8) predicted fault; (9) strike-slip fault; (10) boundary of the basin; (11) River
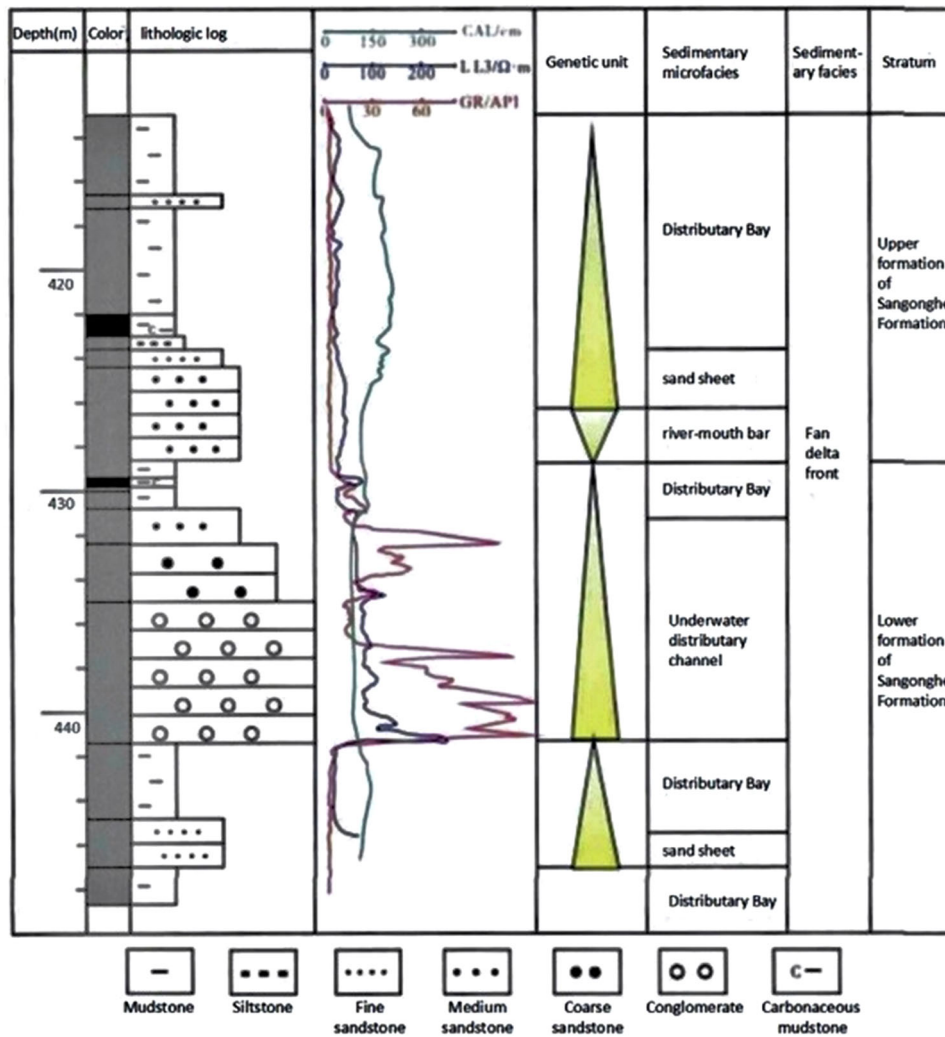
Fig. 2 (Color online) Sedimentary microfacies of the Lower Jurassic Sangonghe Formation [2]
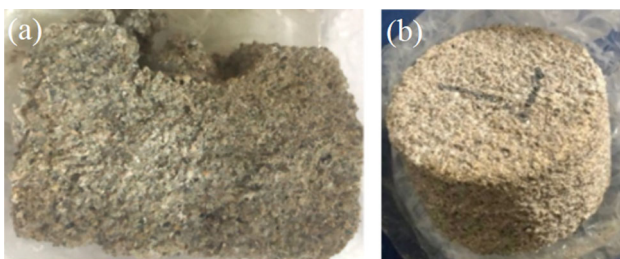

composed of medium-grained sand chips with loose structure. After oxidation and hydrolysis, it is in the shape of "bean curd residue" (Figs. 1–3; Table 1).

Fig. 3 (Color online) Medium-coarse uranium-bearing sandstone rock samples. **a** S1, 65 mm × 43 mm × 32 mm; **b** S7, 59–39 mm

Table 1 Sample information of low-permeability uranium-bearing sandstone

Sample number	Well number	Sampling depth (m)	Porosity[a] (%)	Lithology
S1	J5	429.3	16.39	Grayish white medium sandstone
S7	J9	425.9	12.38	Grayish white medium sandstone

[a]Porosity was measured by the MIP method

2.2 Experimental methods

2.2.1 HPMI testing

HPMI is one of the most commonly used experimental techniques to measure pore throat size distribution and effective porosity. Based on the mercury injection method, the lower limit of fluid flow, throat, and its connected pore volume can be quantitatively evaluated, which is helpful for understanding the law of fluid seepage [46]. An Autopore IV 9500 pore analyzer was used in this HPMI experiment. The test pressure ranges from 0.1 Psia to 33,000 Psia, and the measured pore throat diameter ranges from 360 μm to 5 nm.

The pore throats are assumed to be connected capillary tubes of different diameters, and the permeability of the pore throat of radius r_j is [47, 48]

$$k_j = \frac{\phi_j}{8} r_j^2, \tag{1}$$

where k_j represents the permeability of the pore throat with radius r_j and $\varnothing_j$ is the ratio of the volume of the pore throat with radius r_j to the total pore volume.

The core permeability contribution rate corresponding to a certain radius of the pore throat is characterized by

$$\frac{k_j}{k} = \phi_j r_j^2 / \sum_i^N \phi_i r_i^2. \tag{2}$$

2.2.2 NMR testing

NMR experiments transform the T_2 spectrum of nuclear magnetic resonance into the distribution curve of the pore radius, which can be used to evaluate the pore structure of cores and characterize the pore size distribution at multiple scales [46]. NMR experiments were carried out on the MacroMR12-150H-I core nondestructive and microcosmic testing imaging and analysis system.

2.2.3 XRD testing

XRD can obtain information on the mineral composition, crystal structure, or morphology, through the diffraction patterns of samples, so as to quickly and accurately identify the minerals of ore rocks. A representative portion of the samples (approximately 10 g) was crushed and ground into powder (particle size < 0.2 mm), and the main minerals in the sample were analyzed using a Bruker D8 Advance X-ray diffractometer. The Jade6.0 software was used to analyze the phases of the XRD patterns. After peak division, background value deduction, and smoothing treatment, combined with the geological background of the study area, the phase compositions were retrieved using standard PDF reference cards.

2.2.4 WD-XRF testing

Wavelength-dispersive X-ray fluorescence spectrometer is a type of spectrometer that uses crystal spectrum. It is widely used in the determination of various elements and oxides in geological studies. The WD-XRF spectrometer Axios MAX was used for the quantitative analysis of mineral elements in solid disk samples with a diameter of 38 mm and a thickness of 10 mm.

2.2.5 SEM–EDS experiment

SEM–EDS can automatically identify the mineralogy of each image pixel according to the detected element spectrum with the known chemical compositions and generate a mineral distribution map [31, 39]. The surfaces of the samples were gently polished with 1000, 2000, and 4000 grade polishing paper and then polished to 0.5 μm in a silicon solution. The samples were ultrasonically cleaned in water to remove any silica-like material during polishing and drying. In order to improve the conductivity of the samples under an electron beam, several nanometers of amorphous carbon was sputtered on the surface of the samples.

SEM–EDS experiments were carried out on an FEI Scios™ system, which is equipped with secondary and backscatter electron detectors and silicon drift detectors of the Oxford instrument for EDS. By adjusting the scanning voltage, it was found that the contrast of the SEM images was good at 10 kV, so 10 kV was selected to scan the end face of the sandstone sample in this study. The spot size of the scanning electron microscope image was 10 nm and the working distance was 6.8 mm. EDS mapping images of the same surface were also obtained using AZtec software.

2.2.6 Multi-resolution CT scans

Micro-CT scans are based on the different X-ray absorption coefficients of different density components in the rock, and the computer image reconstruction is used to make the material information of different densities on the designated layer displayed in high-resolution digital images. The low-permeability uranium-bearing sandstone used in this study is easily damaged when sampling with a drill bit because of its low mechanical strength, so the rock sample is embedded in epoxy resin to ensure the strength. Then, samples of 15 mm × 15 mm × 20 mm and 1.5–1 mm microplugs were drilled by bits of different sizes. Micro-CT scans were performed on the nanoVoxel-2000 X-ray CT scanner system produced by Sanying Precision Instrument Co., Ltd. (Tianjin, China), which has a

Table 2 Setting of scanning parameters of micro-CT

Sample	Dimension (mm)	Resolution (μm)	Voltage (kV)	Electric current (uA)	Exposure time (s)
Model	15 mm × 15 mm × 20 mm	12.58	150	150	0.65
Reference	1.5–1 mm	1	80	60	0.7

maximum resolution of 0.5 μm. The basic sample size used for the entire study was rectangular samples of 15 mm × 15 mm × 20 mm. First, the basic samples were scanned by micro-CT with medium resolution (12.58 μm) to observe the overall structure and internal porosity. According to the medium-resolution CT scan results, the volume of interest (VOI) was then selected for further imaging. The locations of the subsamples (1.5–1 mm) were marked and extracted from the basic cores and scanned at a higher resolution (1 μm) to study the finer pore structure. Table 2 shows the settings of the scanning parameters of the micro-CT equipment at different resolutions.

3 Results

3.1 Mineral characteristics of low-permeability uranium-bearing sandstone

3.1.1 Mineral composition and chemical constituents

XRD combined with XRF analysis can improve the accuracy of mineral composition identification. XRD analysis of the samples (Fig. 4) shows that the main minerals in the samples are quartz, ankerite, feldspar, and calcite, followed by clay minerals such as kaolin, illite, and chlorite, and a small amount of metal minerals (owing to the small content, it is not shown in the figure), such as pyrite, rutile, and sphalerite. Clay minerals mainly include kaolinite, illite, and chlorite. Kaolinite is the most

developed, followed by chlorite and illite, which reflects the dissolution of feldspar during diagenesis and mineralization.

The results of petrochemistry analysis of low-permeability uranium-bearing sandstone are shown in Table 3. The $K_2O + Na_2O$ content of the ore-bearing rock samples ranges from 2.88% to 3.30%, and the K_2O/Na_2O value is greater than 1, which indicates that the feldspar clasts in the sandstone are mainly K-feldspar.

Table 3 XRF analysis of low-permeability uranium-bearing sandstone

Compound	Content (%)		Compound	Content (%)	
	S1	S2		S1	S2
SiO_2	45.047	53.865	Cl	0.041	0.039
CaO	25.178	19.387	U	0.036	0.031
Al_2O_3	18.623	16.495	Mo	0.019	0.008
Fe_2O_3	6.875	4.110	Tb_4O_7	0.025	0.030
K_2O	3.290	2.759	Cr_2O_3	0.022	0.032
MnO	0.552	0.714	Na_2O	0.0141	0.019
MgO	0.531	0.881	SrO	0.013	0.016
SO_3	0.248	0.619	Rb_2O	0.013	0.014
TiO_2	0.239	0.398	ZrO_2	0.013	0.017
P_2O_5	0.214	0.491	ZnO	0.011	0.013
CeO_2	0.046	0.057	Y_2O_3	0.003	0.004

Fig. 4 XRD analysis of low-permeability uranium-bearing sandstone. **a** Histogram of minerals relative contents; **b** histogram of clay minerals relative contents
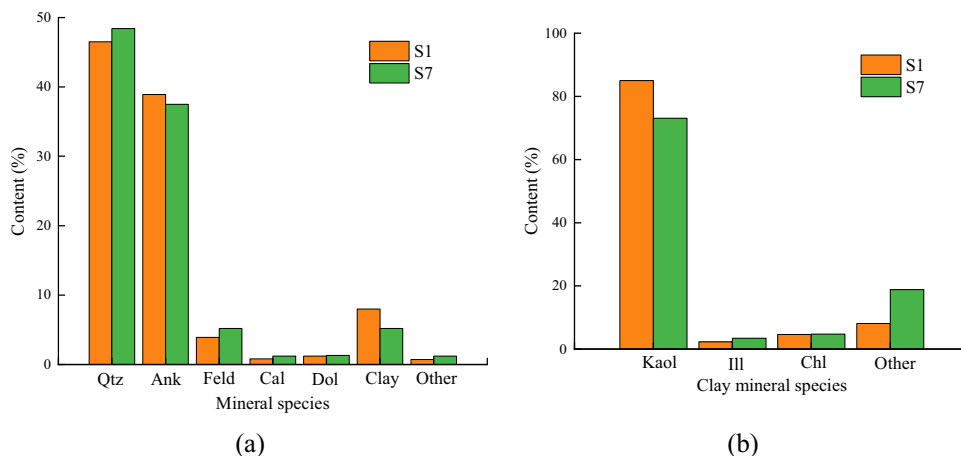
3.1.2 Mineral distribution characteristics

The mineral and pore distribution images of the polished faces were obtained using EDS–SEM analysis. EDS mapping analysis showed the distribution of Si, Al, Ca, Mg, O, C, K, and S (Fig. 5). It can be seen that the main intergranular pores in the rock sample are mainly filled with clays (Al + Si + Mg), while quartz (Si + O), dolomite (Ca + Mg + C), K-feldspar (Si + Al + K), and other particles that constitute the rock sample skeleton are covered with many clays. According to the mineralogical composition and mass fraction in Fig. 5, it can be seen that the relative content of ankerite and dolomite is high, while the relative content of calcite is low, which indicates that there is significant dissolution and metasomatism in the diagenesis of low-permeability uranium-bearing sandstone reservoir [41].
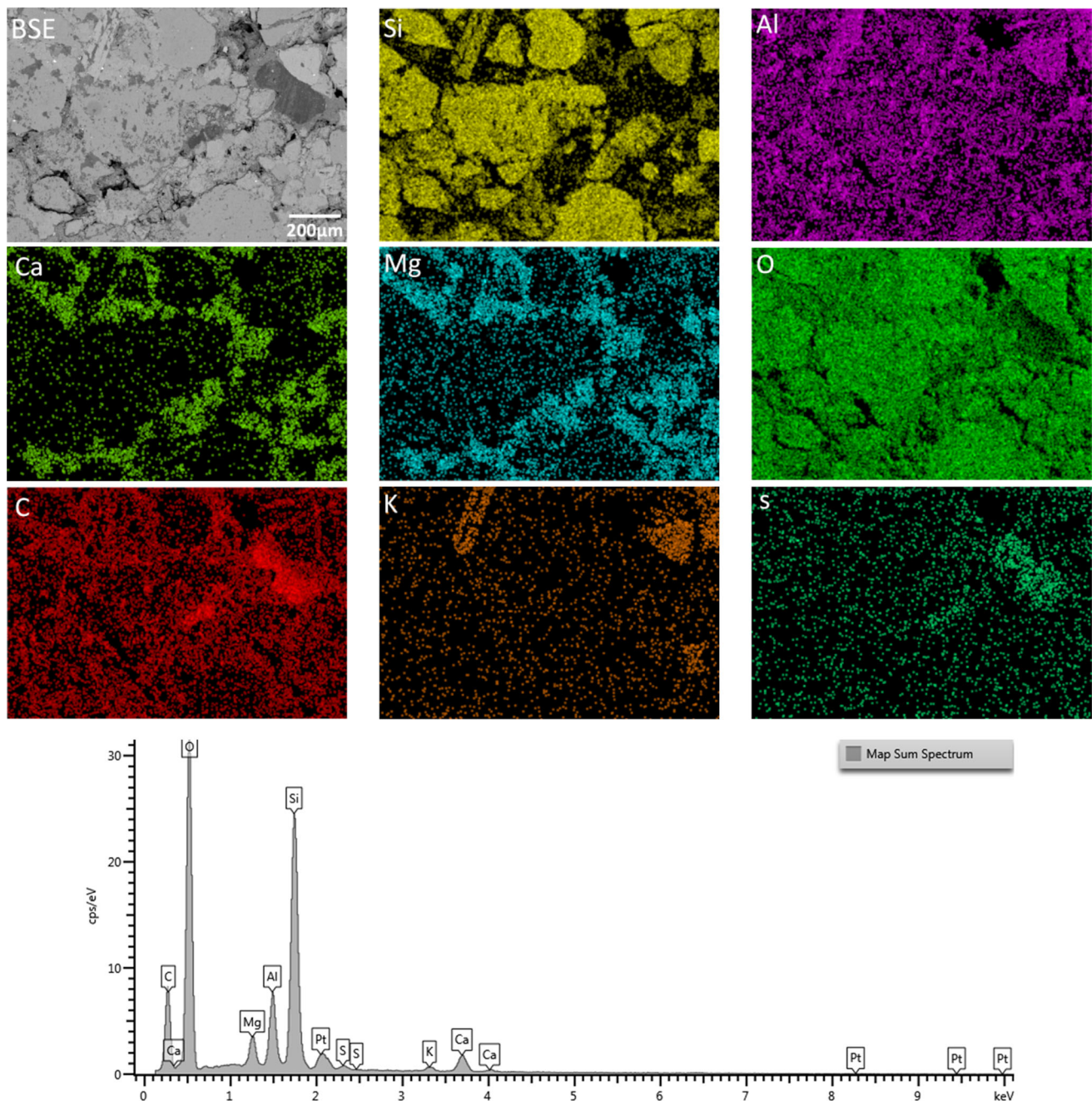

Fig. 5 (Color online) EDS spectrum and map captured from low-permeability uranium-bearing sandstone

Fig. 6 (Color online) BSE images of uranium in low-permeability uranium-bearing sandstone. **a** Coffinite and pyrite in carbonate cements; **b** coffinite precipitate in residual intergranular pores of clay minerals and sandstone interstitial materials; **c** coffinite adsorption on pyrite surface; **d** coffinite occurs in the interstitial materials of quartz and feldspar. *Qtz* quartz; *Cly* clay mineral; *CC* carbonate cement; *Fsp* feldspar; *Cal* calcite; *Py* pyrite; *Cof* coffinite; *Org* organic
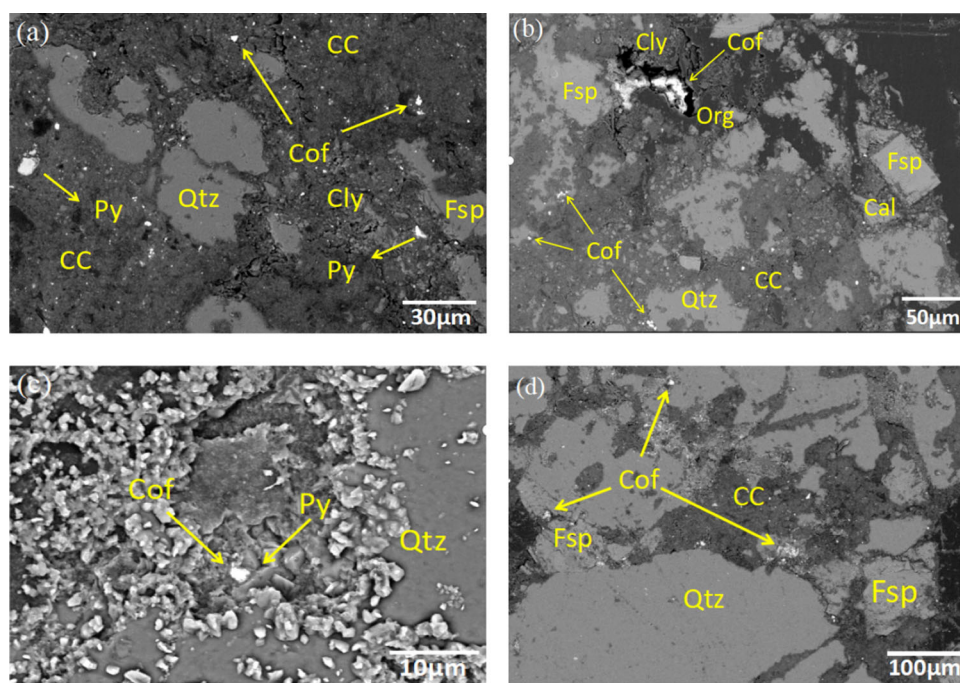
3.1.3 Occurrence state of uranium

Under the SEM, uranium minerals are mostly bright white, and the particles are small and scattered in the rock minerals. In addition, coffinite often coexists with pyrite and disperses in sandstone cements in clumps (Fig. 6a). The BSE image shows that the irregular pyrite grains are mainly distributed around clastic quartz and rock debris, while star point pyrite is mainly distributed in cement and clay minerals (Fig. 6a). Due to the strong adsorption of clay minerals, coffinite is absorbed by clay minerals and then precipitated around the clay membrane or in clay minerals (Fig. 6b). Coffinite also exists on the surface of pyrite and in intergranular pores (Fig. 6c). Moreover, some intact coffinite occurs in the middle of clastic grains such as feldspar, which should be carried from the provenance area (Fig. 6d).

3.2 Pore structure characteristics of low-permeability uranium-bearing sandstone

3.2.1 Pore structure types

The pore types and genesis of low-permeability uranium-bearing sandstone were analyzed by micro-CT scanning and SEM. It can be seen that there are four main pore types in the cores of low-permeability uranium-bearing sandstone, which include intergranular pores, intragranular dissolution pores, intercrystalline micropores, and micro fractures, as shown in Fig. 7. Among them, intergranular pores mainly include intergranular pores of detrital minerals and intergranular dissolution pores. The number of intergranular pores of clastic minerals is small, but the spatial scale is relatively large, and most of them are in the shape of narrow triangles or multilateral shapes with smooth straight edges (Fig. 7a). The intergranular pores of clastic minerals were altered by diagenesis, such as mechanical compaction or cemented filling of clay minerals, resulting in a large number of micro–nanoscale intergranular dissolution pores (Fig. 7b). The dissolution pores are mainly secondary pores produced by carbonate particles, feldspar particles, and interstitials (kaolinite, chlorite) formed by dissolution. Dissolution pores within the grains are widely developed and have irregular pore surfaces with diameters ranging from a few nanometers to a few microns (Fig. 7c, d, e). Intergranular micropores are mostly formed by authigenic minerals and clay minerals in rocks (Fig. 7f, g) with small pore diameters. Micro fractures mainly exist in carbonate minerals and are formed by dissolution as well as brittle mineral fracture and clay mineral shrinkage (Fig. 7h, i) with a width of less than ten nanometers and up to several hundred microns. The existence of micro fractures enhances the connectivity of reservoir pores, increases the permeability, and plays an important role in the drainage of the solution. In summary, it can be seen that in the samples, even the same mineral may contain multiple pore types. The pore structure of low-
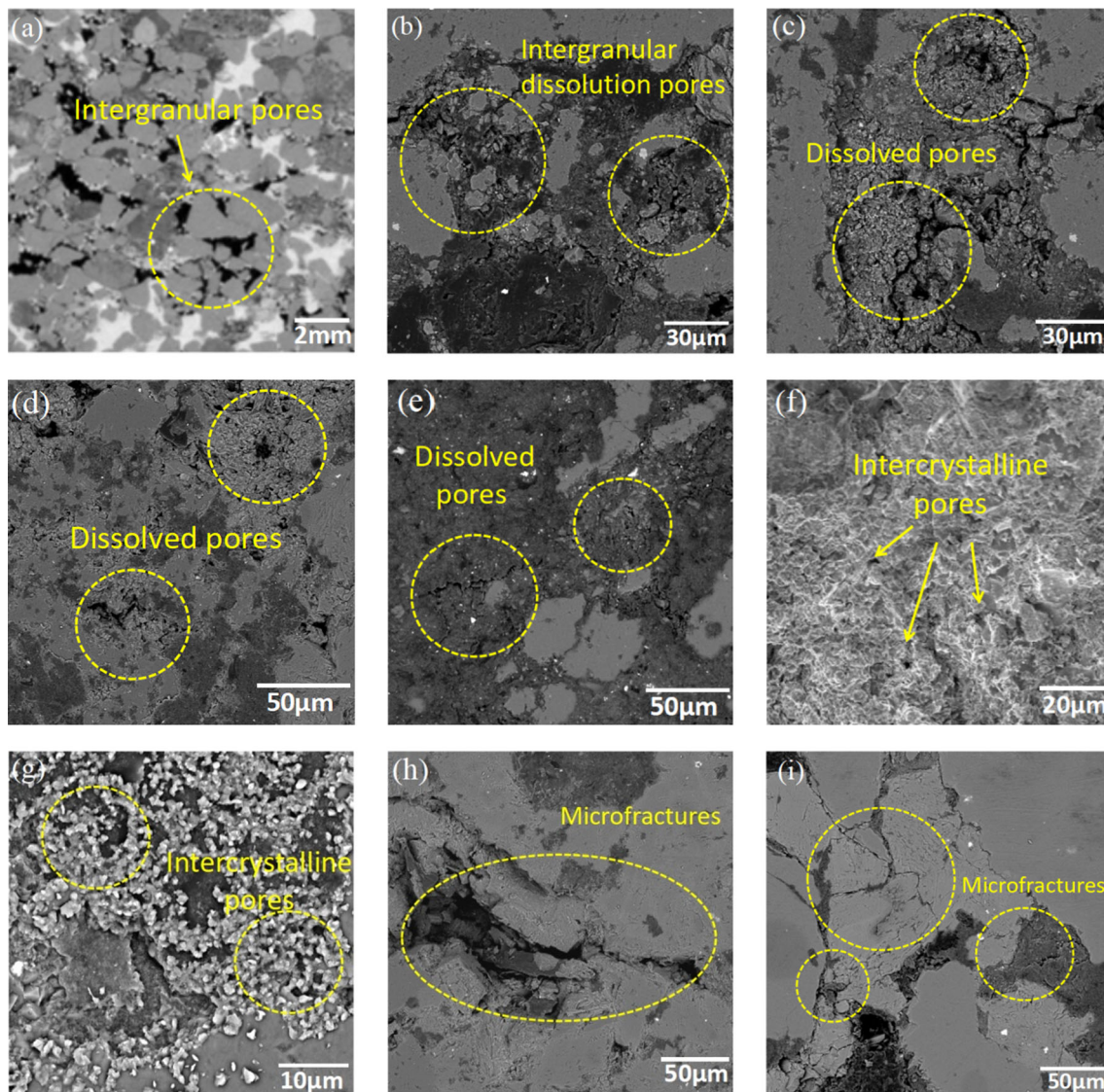
Fig. 7 (Color online) Representation of the typical pore types in low-permeability uranium-bearing sandstone: **a** intergranular pore of clastic minerals, CT; **b** intergranular dissolution pores between quartz and kaolinite, BSE; **c** intragranular pores formed by dolomite dissolution, BSE; **d** intragranular dissolution pores formed by feldspar dissolution, BSE; **e** intragranular dissolution pores formed by kaolinite dissolution, BSE; **f** intercrystalline pores in kaolinite, SEM; **g** intercrystalline pores in pyrite, BSE; **h** micro fractures formed by brittle mineral fracture, BSE; **i** microfractures formed by shrinkage of clay minerals, BSE

permeability uranium-bearing sandstone is complex and has multi-scale characteristics.

3.2.2 Pore throat size distribution analysis by MIP

The MICP data show that the pore throat sizes of low-permeability uranium-bearing sandstone vary from millimeter to micrometer. According to the diameter, the term "micropore throat" is applied to pore throat sizes less than 1 μm, "mesopore throat" is the term applied to pore throat sizes less than 10 μm, and "macro pore throat" is the term applied to pore throat sizes greater than 10 μm [49, 50]. Based on the statistics of the influence of different pore-throat sizes on the permeability of the samples, it was found that the contribution of permeability of the samples mainly comes from the large throat (99.51%), and it can be inferred that the large pore throat has good connectivity (Fig. 8).
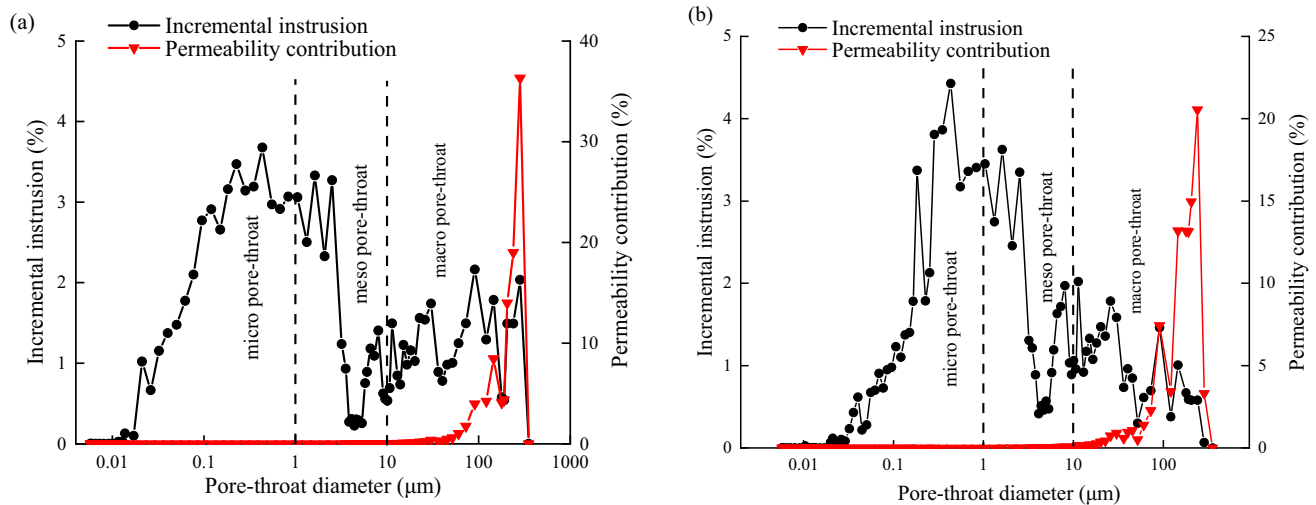
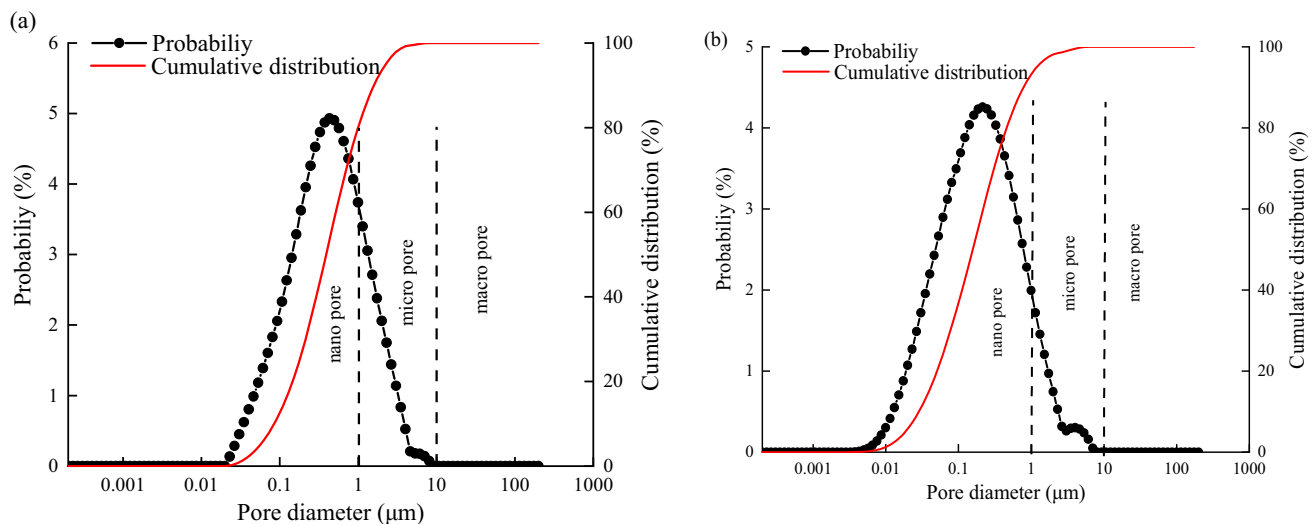Fig. 8 (Color online) MICP pore throat size distribution: **a** S1; **b** S2

Fig. 9 (Color online) NMR pore size distribution: **a** S1; **b** S2

3.2.3 Pore size distribution analysis by NMR

The NMR test results of the samples were converted into pore diameter distributions, as shown in Fig. 9. The pore diameter of the samples is in the range of 50–300 μm. Although the seepage ability of micropores is small, the pore volumes of the nanopores and micropores are larger. The micropores are not easily wetted and permeated by the lixivium, which limits the free flow and permeability of the lixivium in its interior. Moreover, the influence of clay minerals on porosity and pore flow capacity cannot be ignored when clay minerals disperse into fine particles along with the flow of lixivium and block micropores.

3.3 Construction and evaluation of low-permeability uranium-bearing sandstone digital core

In this study, the CT data were analyzed using the 3D visualization software Avizo 9.0.3. First, the contrast of the CT images is adjusted and the signal-to-noise ratio is boosted by a non-local means filter, so as to optimize the images into a mode that is more suitable for identification and analysis. According to the X-ray attenuation characteristics of different minerals, the mineral phases whose gray values differ greatly can be directly identified from the tomographic images [12, 14]. For example, the high density pyrite is bright white in the CT image. The clay minerals, quartz, and feldspar can be identified because of the large difference in gray values. It can be seen that the

Fig. 10 (Color online) CT scan results of low-permeability uranium-bearing sandstone cores at different resolutions. **a** 2D slice from medium resolution CT scan voxel size: 12.58 μm. **b** 2D slice from high resolution CT scan, voxel size: 1 μm. *Qtz* quartz; *Cly* clay mineral; *Fsp* feldspar; *Dol* dolomite; *Ank* ankerite; *Kaol* kaolinite
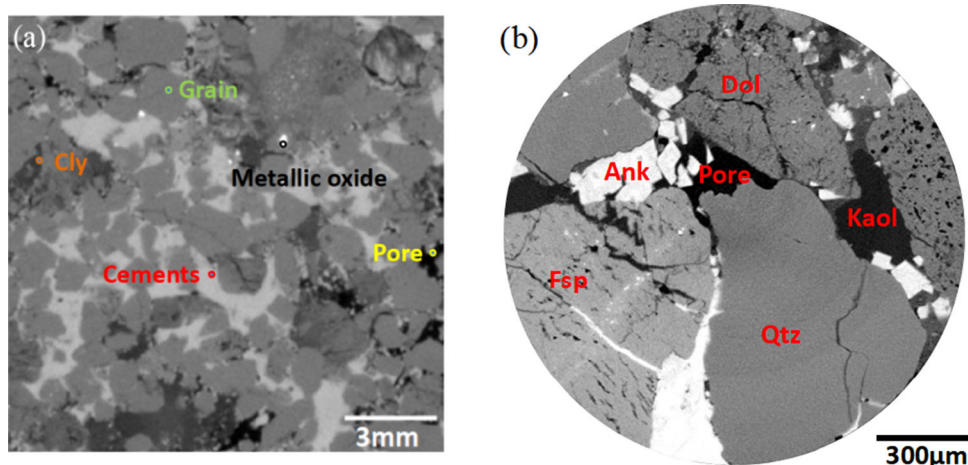
medium-resolution CT scan is helpful for obtaining a basic understanding of the internal structure of rocks over a large range (Fig. 10a). For example, there is a large amount of carbonate cements and clay minerals that may have a great influence on the total porosity and permeability in low-permeability uranium-bearing sandstone. High-resolution CT images can identify micropores and obtain better image quality (Fig. 10b). At the same time, the correlation between quartz particles, feldspar, and clay minerals is significant in the high-resolution images, which is conducive to separating minerals from the skeleton. In order to establish a digital core model that can accurately reflect the pore structure characteristics of reservoir rocks, two types of resolution CT images can be registered in space to find the corresponding position of the subsample image in the plunger sample image and form multi-scale core scanning images.

3.3.1 Image registration

Image registration is a necessary preliminary procedure for multi-image fusion. The feature-based image registration method uses the feature points of the image to achieve image registration. Firstly, the interested image features are detected by the feature extraction operator. Secondly, the feature matching algorithm is used to select the feature pairs with matching relationships in the corresponding feature set of two images. Then, the transformation model between images is calculated by using the coordinate relationship between pairs feature parameters to achieve image registration [51]. The main goal of spatial registration of different resolution 3D CT images is to align and overlap the two-image data into the same coordinate system.

In this study, registration with the landmarks algorithm provided by FEI Avizo was used to register CT images of low-permeability uranium-bearing sandstone with different resolutions. In registration, typically a low-resolution CT image data set is taken as the reference, and the model of high-resolution CT image data sets is transformed, moved, and possibly rescaled, until both data sets match. According to the location of the pre-marked subsample, the converter of the *Transform Editor* was used to translate, rotate, and scale the reference image, so that the model image was roughly aligned with the reference image. Landmark sets were then artificially selected and created to calculate the transformation equation matching the landmark sets. Using the *Tcl* command in Avizo console, the numerical values of the registration transformation can be retrieved. Owing to the distortion of the image in the process of sampling, the simple rigid body transform algorithm cannot satisfy the registration of the images. Therefore, the Bookstein image distortion algorithm was used to register the images fine. The points in the transformed group (model) were forced to fit to the reference points, and all image points in between were shifted by using the correlation of the surrounding points to achieve the best image registration [14, 52]. After verification and confirmation of overlapping known features, the registration is successful, and features (texture, crack, void) with the same coordinates are found on the final registered image (Fig. 11c, d).

3.3.2 Pore segmentation

After fusion, CT images have both high- and low-resolution image data. For medium-resolution CT images, owing to the serious marginal fuzzy effect of pores and skeletons, they cannot be simply divided by the binary method [53]. The K-means method is a purely stochastic technique that estimates G_{min} and G_{max} based only on the gray-level distribution of the 3D microtomography images [24, 54]. Using the two threshold levels G_{min} and G_{max} estimated by the K-means algorithm, the gray level of the CT image can be divided into three segments: pores,
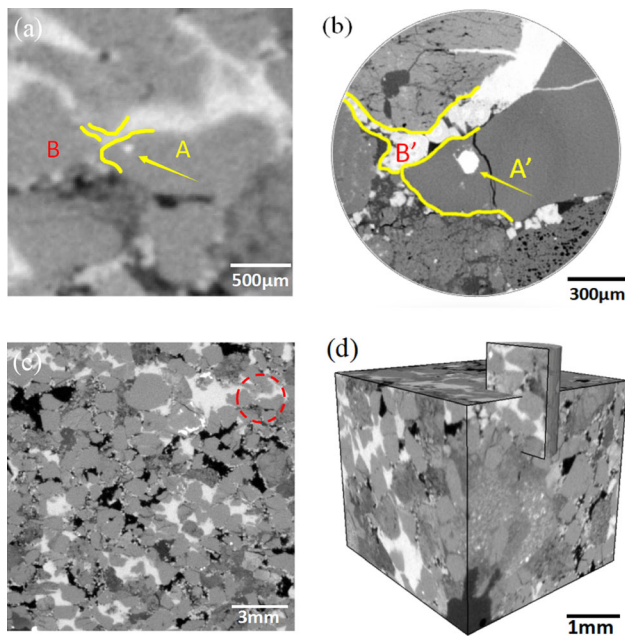
Fig. 11 (Color online) 3D-to-3D image registration: **a** registration surface of medium-resolution CT; **b** registration surface of high-resolution CT, yellow curves indicate possible points for landmarks (A, A′ and B, B′); **c** 2D registration of cross sections between core and sub-sample, red curve indicates the landmarks of the core and sub-sample, **b**, **d** 3D registration between sub-sample and core
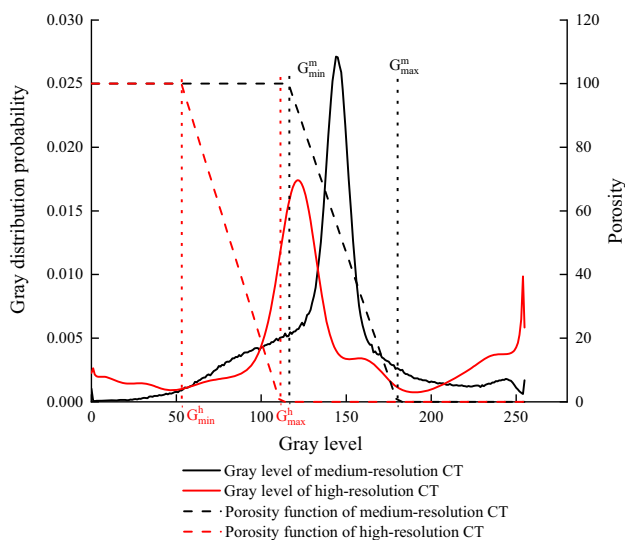

Fig. 12 (Color online) Porosity linear functions and the probability distribution functions of gray levels of different resolution CT images

skeleton, and unresolved pores. The linear function of the porosity and probability distribution function of the grayscale of CT images with different resolutions are shown in Fig. 12. By calculating the G_{min} and G_{max} of the high-resolution voxel corresponding to the low-resolution voxel, and changing the gray value of G_{min} of the low-resolution CT image, although the pores and skeletons
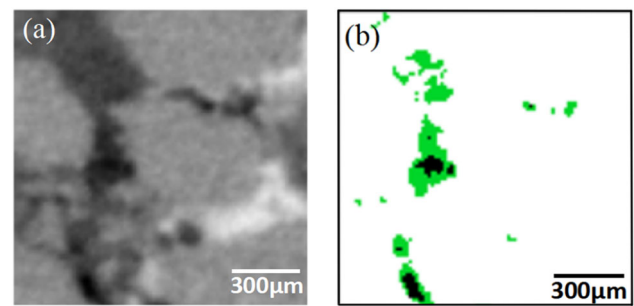

Fig. 13 (Color online) Pore segmentation results of low-resolution image: **a** medium-resolution CT image; **b** the segmentation result of medium-resolution CT images combined with high-resolution CT segmentation threshold, black represents the pores obtained from conventional binary segmentation, and green represents the pores after fusing the segmentation threshold G_{min} of high-resolution CT image

cannot be completely accurately divided, the overlapped gray levels in the low-resolution CT image can be better segmented and the pore characteristics of diameter greater than 1 μm in the high-resolution CT image can be fused [16]. Indeed, the contribution of the macro throat (> 10 μm) to the permeability of the sample in this test is dominant, and that of the micro throat (< 1 μm) can almost be ignored, so the digital core pore model established after integrating the pores of the high-resolution CT image meets the reliability of the next permeability simulation analysis.

Finally, the three-dimensional digital core pore model of the plunger sample is obtained, as shown in Fig. 13. It can be seen from Fig. 8b that the pore connectivity in the medium-resolution CT image has been significantly improved after the fusion of the pores identified by the high resolution.

3.3.3 Skeleton segmentation

Owing to the blurring of edges caused by noise and volume effects in the process of image acquisition and reconstruction, the commonly used simple threshold segmentation method often produces inaccurate or even wrong segmentation results, especially in the phase transition region where more than two phases are segmented. Watershed segmentation can effectively solve these problems in many cases. The principle and operation of watershed segmentation are introduced in detail in [36, 45], which will not be repeated here. However, watershed segmentation is prone to undersegmentation or oversegmentation, and the segmentation results usually have some errors with the measured values.

BSE images have the advantages: high resolution, clear microscopic component morphology, and those can be combined with energy spectrum analysis (EDS) to identify
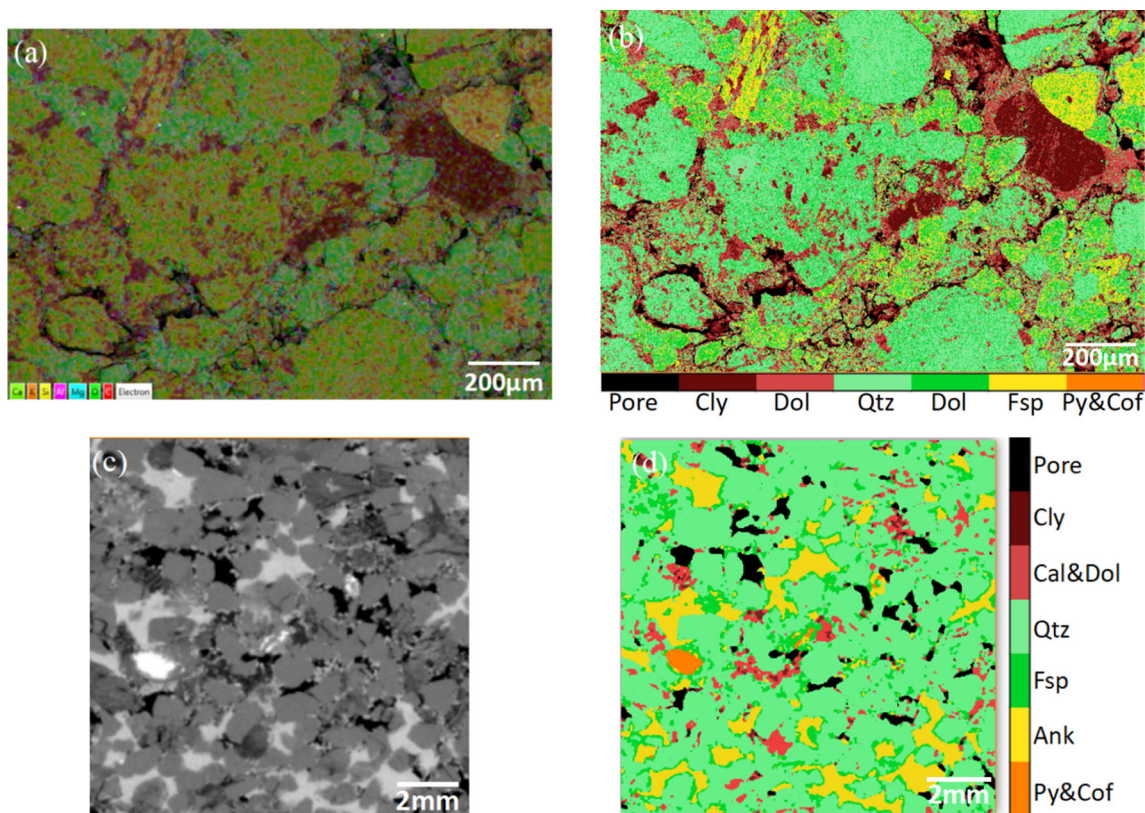
Fig. 14 (Color online) 2-D image of **a** EDS image; **b** segmented micro BSE image; **c** CT image; **d** segmented CT image. *Qtz* quartz; *Cly* clay mineral; *Cal* calcite; *Dol* dolomite; *Fsp* feldspar; *Py* pyrite; *Cof* coffinite

minerals. At the same time, the gray value of the SEM image pixels is related to the density of rock samples, so it can be used to verify the distribution of gray values of different mineral components in CT images [38, 55, 56]. In this study, SEM images, EDS spectra, and maps were used to calibrate the threshold segmentation of different components of the CT image. The SEM image obtained in this study is an eight-bit grayscale image. The *histogram* tool in ImageJ software was used to quantitatively count the gray range of each component in the sample, and the average value was obtained. The segmentation thresholds of pyrite and coffinite, feldspar, dolomite, quartz, dolomite, clay minerals, and pores are 242–255, 173–241, 172–146, 105–145, 104–85, 54–85, and 0–53, respectively.

Because the gray value in CT images depends on the density of each mineral phase, it is difficult to distinguish between two minerals with similar densities, such as calcite and dolomite. In this study, the CT images were divided into seven phases, namely pore space, clay minerals, calcite/dolomite, quartz, ankerite, feldspar, pyrite, and coffinite for further analysis and volume performance simulation. Comparing the sample EDS spectrum and map with the segmentation threshold of watershed segmentation, reasonable segmentation thresholds of minerals are obtained. Multi-mineral SEM images after watershed

segmentation are shown in Fig. 14b. Compared with the EDS image (Fig. 14a), it can be seen that good segmentation results can be obtained by using this method. The mineral skeleton of high-resolution CT images is also divided by watershed segmentation. The threshold value of each mineral in the CT image was determined by comparing the gray value and segmentation threshold of the BSE image. The multi-mineral images of CT after watershed segmentation are shown in Fig. 14d.

3.3.4 Digital core evaluation

A variety of morphological algorithms in Avizo Fire are applied to quantitatively characterize the micropore characteristics and mineral content proportion of low-permeability uranium-bearing sandstone. The fast watershed algorithm was used to mark the pores, and each pore was quantitatively analyzed. According to the volume of marked pores, the porosity of the digital core could be obtained [25, 57–59]:

$$\phi = \frac{\sum V_{\mathrm{P}}}{V_{\mathrm{v}}}, \tag{3}$$

where V_{P} is the single pore volume, pix^3, and V_{v} is the total volume, pix^3.

Table 4 Porosity of low-permeability uranium-bearing sandstone

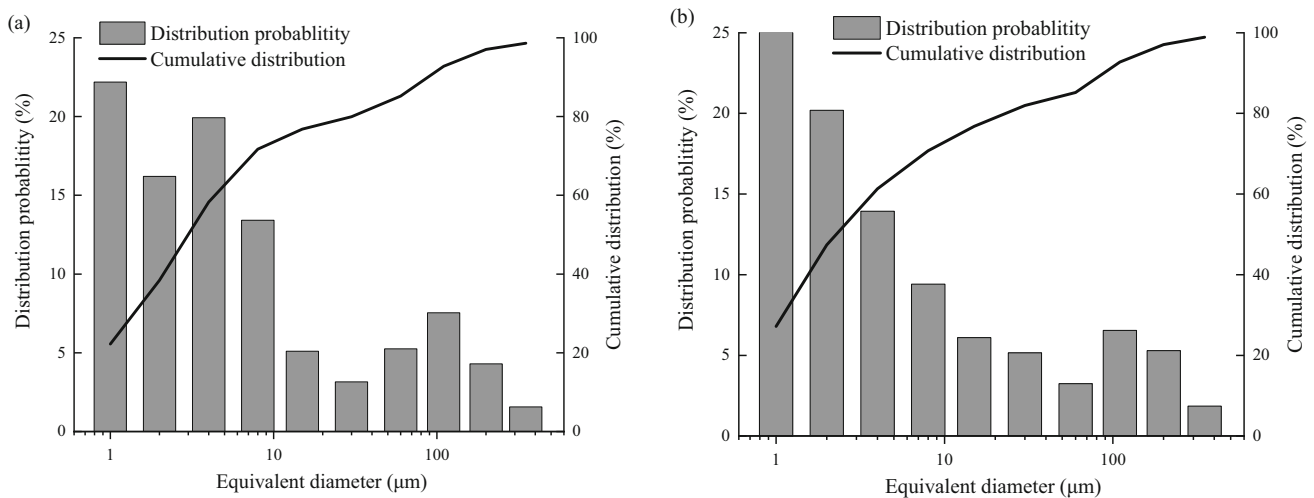| Sample	Porosity (%)										
	Low resolution CT		Total	High resolution CT		Total	Fusion CT		Total	HPMI
	Open pore	Close pore		Open pore	Close pore		Open pore	Close pore		
S1	6.82	1.21	8.03	8.26	4.23	12.49	9.12	5.06	14.72	16.39
S2	5.45	1.03	6.48	5.82	3.51	9.33	6.48	4.59	11.07	12.38

Fig. 15 Equivalent diameter of pore size distributions based on micro-CT images: **a** S1; **b** S2

On the basis of the 3D digital core pore model, isolated pores can be removed by using four connected region labeling algorithms, and connected pores can be obtained [60]. The porosity of open pores and close pores can be calculated according to formula (3). It can be seen that the CT images combined with the two resolutions can identify more pores, which is helpful to build an accurate digital core (Table 4).

According to the principle of equivalence, the equivalent pore diameter of each marked pore can be obtained [25]:

$$d_{eq} = \sqrt[3]{\frac{3V_p}{2\pi}}, \tag{4}$$

where d_{eq} is the equivalent pore diameter, pix.

The histogram of the equivalent pore diameter distribution is shown in Fig. 15. Due to the limitation of CT resolution, pore sizes with a diameter of less than 1 μm were not counted, but the distribution of pore size with a diameter of more than 1 μm is in good agreement with the results of the NMR test (Fig. 9).

Table 5 Mineral composition and relative content ratio of core samples

Sample	Methods	Quartz	Ankerite	Feldspars	Calcite	Dolomite	Clays			Metallic minerals
							Kaolinite	Illite	Chlorite	
S1	XRD	46.5	38.9	3.9	0.8	1.2	5.4	0.1	0.5	0.7
	Digital core	51.4	30.17	3.6	7.1		6.8			1.1
S2	XRD	48.4	37.5	5.2	1.2	1.3	3.6	1.5	0.1	1.1
	Digital core	45.9	36.7	4.6	5.4		6.8			0.6

Similar to the porosity, according to the volume of the marked minerals, the proportion of mineral components of the digital core can be obtained. The proportions of the six mineral phases are listed in Table 5. It can be seen that the digital core mineral volume fraction is consistent with the results of the XRD measurement, and the structural information of different components of the core is reconstructed.

4 Discussion

The multi-scale and multi-component digital core overcomes the difficulty of balancing the resolution and core size of the single-scale digital core model and can not only represent the microscopic pore structure of the core, but also describe the macroscopic heterogeneity of the rock sample [53]. The 3D spatial distribution of pores, clay minerals, ankerite cements, pyrite, and coffinite is extracted from the established digital core of low-permeability uranium-bearing sandstone, as shown in Fig. 16c, d, e, f. It can be seen from Fig. 16c that the pore distribution in the samples has microscopic heterogeneity characteristics. The primary pores in the area with flaky or banded distribution and relatively rich are mainly related to the residual intergranular pores or large intergranular dissolution pores, and the secondary pores in the area with isolated distribution that are relatively dispersed are mainly related to the intergranular dissolution pores. Combined with the 3D connected pore distribution in Fig. 16g, it can be seen that the intergranular pore forms the main seepage channel in the pore space of the low-permeability uranium-bearing sandstone, and the secondary pore has poor connectivity with other pores [61, 62]. That is to say, intergranular pores mainly provide flow pores and seepage capacity, which is consistent with the conclusion that the contribution of permeability in the samples is mainly from the large throat obtained by the mercury injection experiment.

By comparing Fig. 16j, k, l of the 3D distribution images of the connected pores and pyrite and coffinite, clay minerals, pyrite, coffinite and pyrite, and coffinite and iron

dolomite, it can be seen that pyrite and coffinite are isolated from the connected pores and surrounded by a large number of clay minerals and ankerite cements, which increases the difficulty of uranium leaching.

Based on the 3D connected digital core model, the pore network model extracted by the maximum sphere algorithm can provide the 3D topological and geometric characteristics of the pore space [63, 64]. The connectivity of the model can be determined by counting the coordination number, which refers to the number of contacts a pore has with its neighbors [36]. The pore network model and its coordination number distribution of low-permeability uranium-bearing sandstone under different conditions are shown in Figs. 17 and 18.

The content, diagenetic variation, and occurrence of clay minerals are important factors affecting the porosity and permeability of sandstone. From the 3D distribution of pores and clays in Fig. 16h, it can be seen that the clays are filled in the primary and secondary pores and pore throats of the samples. When the clay minerals were removed, the coordination number of pores in the pore network model increased, and the connectivity of pores improved (Fig. 18).

Combined with Figs. 16i, 17c, and 18, it is found that the connectivity of the internal pores of the low-permeability uranium-bearing sandstone is strongly affected by a large amount of ankerite cement, and the pore connectivity was significantly improved after the removal of ankerite cements. It can be seen that the low overall permeability of the core is related to the dense ankerite cements filled in a large number of internal pores.

In conclusion, it is known that the high relative content of clay minerals and ankerite cement in low-permeability uranium-bearing sandstone is an important factor affecting the permeability and leaching effect of ore and rock. The corresponding lixivium can be designed and prepared to accelerate the dissolution of clay minerals and dolomite, and more specific leaching tests can be carried out to deepen the leaching mechanism. After being verified by a condition test or an extended test, the research results can be applied to in situ leaching of low-permeability uranium mines.
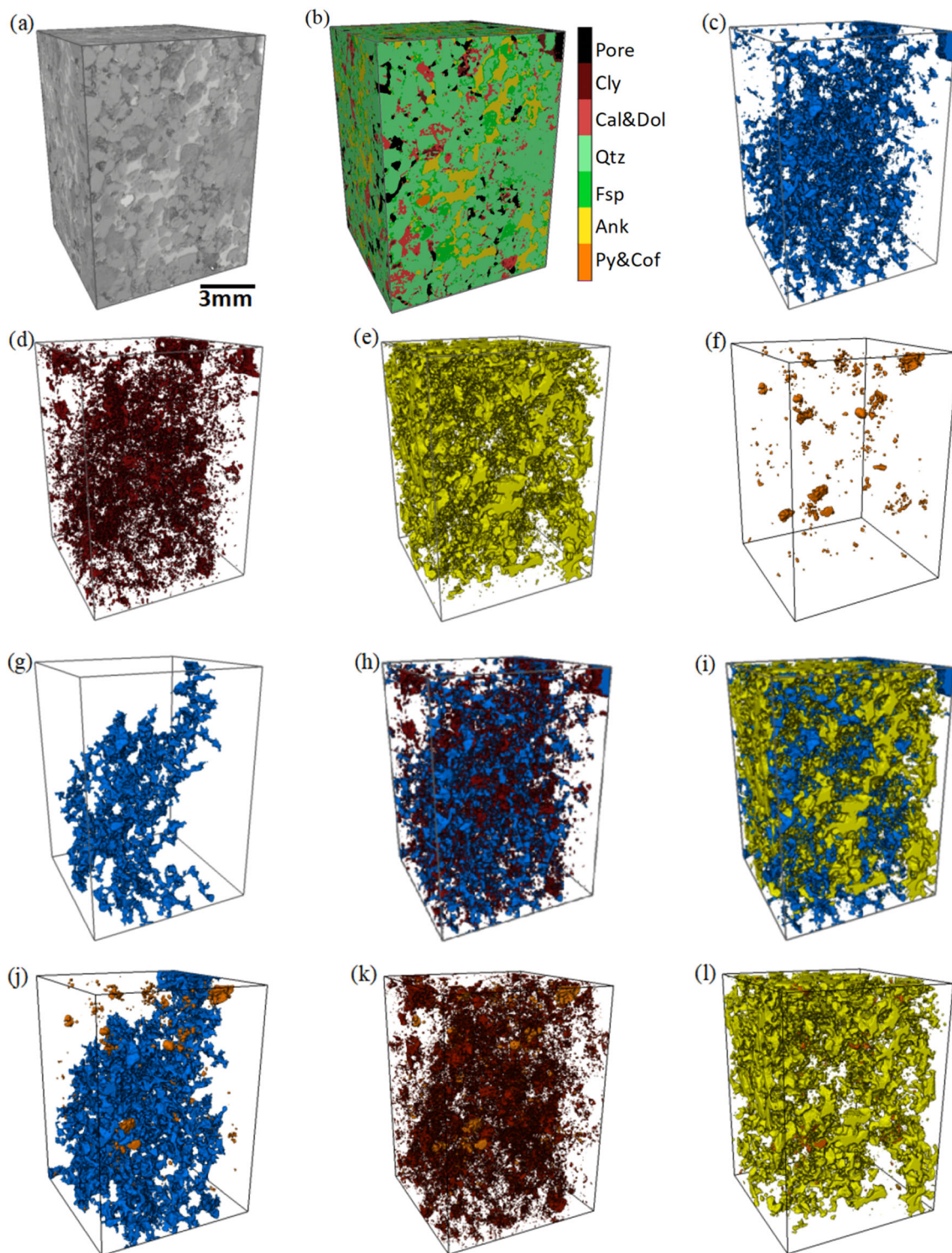
Fig. 16 (Color online) 3D visualization of **a** gray image of the sample; **b** digital core of low-permeability uranium-bearing sandstone; **c** pore distribution; **d** clays distribution; **e** ankerite cements distribution; **f** pyrite and coffinite distribution; **g** connected pore distribution; **h** pore and clays distribution; **i** pore and ankerite cements distribution; **j** connected pore and pyrite and coffinite distribution; **k** clays and pyrite and coffinite distribution; **l** ankerite cements and pyrite and coffinite distribution. *Qtz* quartz; *Cly* clay mineral; *Cal* calcite; *Dol* dolomite; *Fsp* feldspar; *Py* pyrite; *Cof* coffinite
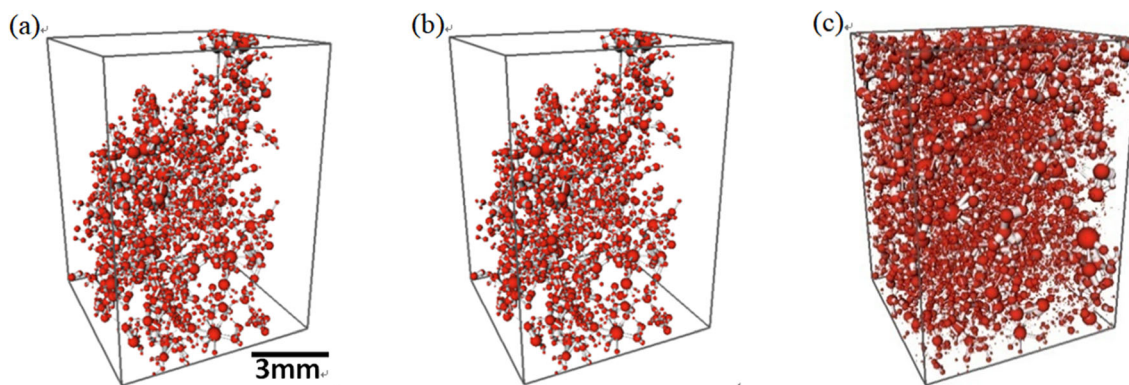
Fig. 17 (Color online) 3D visualization of pore-throat network model: **a** pore-throat network model of connected pore; **b** pore-throat network model of pore without clays; **c** pore-throat network model of pore without ankerite cements
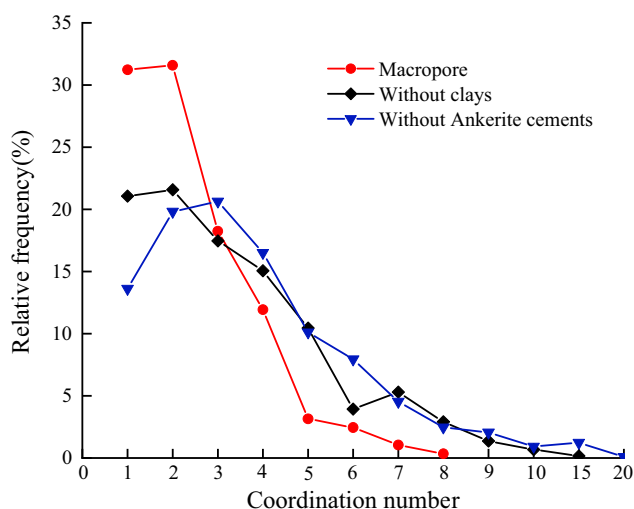

Fig. 18 (Color online) The coordination number distribution of different pore-throat network model

5 Conclusion

To better understand the effect of pore structure and mineral distribution on the seepage characteristics of low-permeability uranium-bearing sandstone, multi-scale and multi-component low-permeability uranium-bearing sandstone digital core is reconstructed by fusing different scale CT image information and EDS–SEM images in this paper. The pore distribution of the reconstructed digital core is in good agreement with the NMR results, and the mineral volume fraction of the digital core is in high agreement with the XRD results, which can truly reduce the structural information of different components of the core.

The porosity of low-permeability uranium-bearing sandstone was quantitatively and qualitatively analyzed by MICP, NMR, and SEM. The results show that there are four main pore types in the cores of low-permeability uranium-bearing sandstone, which include intergranular pores, intragranular dissolution pores, intercrystalline micropores and micro fractures, and even the same mineral in the sample may contain multiple pore types. The pore structure of low-permeability uranium-bearing sandstone is complex and has multi-scale characteristics.

Connectivity analysis of the 3D digital core shows that the intergranular pores determine the main seepage channel in the pore space of low-permeability uranium-bearing sandstone, and the secondary pores have poor connectivity with other pores. This is consistent with the conclusion that the contribution of permeability in the low-permeability uranium sandstone sample is mainly from the macro throat obtained by mercury injection experiment.

Pyrite and coffinite in low-permeability uranium-bearing sandstone are isolated from the connected pores and surrounded by a large number of clay minerals and ankerite cements, which increases the difficulty of uranium leaching. Moreover, the high content of clays and ankerite cements is filled in the primary and secondary pores and pore throats of the samples, which significantly reduces the porosity of the movable fluid in tight sandstone, resulting in the low overall permeability of the core.

The multi-scale and multi-mineral digital core proposed in this study provides a basis for characterizing the macroscopic and microscopic pore and pore-throat structure and mineral distribution of low-permeability uranium-bearing sandstone. In the numerical simulation, the pore structure can be extracted for seepage simulation, and one or several mineral components can be selectively extracted for physical property simulation. It is an important research direction to simulate the scaled-up physical properties of reservoir rocks using a multi-scale digital core model.

References

1. S. Zeng, N. Zhang, S.W. Zhang et al., Fractal characteristics of uranium-bearing sandstone structure and their effects on acid leaching. Energy Sci. Eng. **7**, 1852–1866 (2019). https://doi.org/10.1002/ese3.396

2. F.X. Chen, F.J. Nie, C.Y. Zhang et al., Sedimentary facies of the Lower Jurassic Sangonghe Formation and its relationship with uranium mineralization in Mengqiguer area of Yili Basin, Xinjiang. J. Palaeog. **18**, 833–842 (2016). https://doi.org/10.7605/gdlxb.2016.05.063 (**in Chinese**)

3. B.R. Song, H. Sun, S.L. Yang et al., Characteristics and uranium mineralization of ore bearing rock seriesin Qianjiadian sandstone-type uranium deposits, Songliao Basin. J. Palaeogeog. Chin. **22**, 309–320 (2020). https://doi.org/10.2113/econgeo.106.5.835 (**in Chinese**)

4. H. Song, S.H. Ni, M.C. Hou et al., The characteristic of clay minerals in sandstone-type uranium deposit in the Yili Basin, NW China and its relationship with uranium mineralization. Acta Geol. Sin. **90**, 3352–3366 (2016). https://doi.org/10.3969/j.issn.0001-5717.2016.12.005 (**in Chinese**)

5. Z.M. Yang, X.L. Zhao, C.S. Xiong et al., Research progress on microstructure characterization of pore throat for tight oil reservoirs. Sci. Tech. Rev. **37**, 89–98 (2019). https://doi.org/10.3981/j.issn.1000-7857.2019.05.012 (**in Chinese**)

6. X.H. Shao, X.Q. Pang, F.J. Jiang et al., Reservoir characterization of tight sandstones using nuclear magnetic resonance and incremental pressure mercury injection experiments: implication for tight sand gas reservoir quality. Energy Fuel. **31**, 10420–10431 (2017). https://doi.org/10.1021/acs.energyfuels.7b01184

7. H.W. Zhou, J.C. Zhong, W.G. Ren et al., Characterization of pore-fracture networks and their evolution at various measurement scales in coal samples using X-ray μCT and a fractal method. Int. J. Coal. Geol. **189**, 35–49 (2018). https://doi.org/10.1016/j.coal.2018.02.007

8. H.X. Huang, W. Sun, W.M. Ji et al., Effects of pore-throat structure on gas permeability in the tight sandstone reservoirs of the Upper Triassic Yanchang formation in the Western Ordos Basin, China. J Petrol. Sci. Eng. **162**, 602–616 (2017). https://doi.org/10.1016/j.petrol.2017.10.076

9. J. Lai, G.W. Wang, Z.Y. Fa et al., Insight into the pore structure of tight sandstones using NMR and HPMI measurements. Energy Fuel. **30**, 10200–10214 (2016). https://doi.org/10.1021/acs.energyfuels.6b01982

10. M. Schmitt, C.P. Fernandes, F.G. Wolf et al., Characterization of Brazilian tight gas sandstones relating permeability and Angstrom-to micron-scale pore structures. J. Nat. Gas. Sci. Eng. **27**, 785–807 (2015). https://doi.org/10.1016/j.jngse.2015.09.027

11. J. Klus, P. Mikysek, D. Prochazka et al., Multivariate approach to the chemical mapping of uranium in sandstone-hosted uranium ores analyzed using double pulse laser-induced breakdown spectroscopy. Spectrochim. Acta. B. **123**, 143–149 (2016). https://doi.org/10.1016/j.sab.2016.08.014

12. Z.L. Cheng, Z.F. Ning, H.W. Zhao et al., A comprehensive characterization of North China tight sandstone using micro-CT, SEM imaging, and mercury intrusion. Arab. J. Geosci. **12**, 407 (2019). https://doi.org/10.1007/s12517-019-4568-9

13. A. Kazak, S. Chugunov, A. Chashkov, Integration of large-area scanning-electron-microscopy imaging and automated mineralogy/petrography data for selection of nanoscale pore-space characterization sites. Spe. Reserv. Eval. Eng. **21**, 821–836 (2018). https://doi.org/10.2118/191369-Pa

14. W. De Boever, H. Derluyn, D. Van Loo et al., Data-fusion of high resolution X-ray CT, SEM and EDS for 3D and pseudo-3D chemical and structural characterization of sandstone. Micron **74**, 15–21 (2015). https://doi.org/10.1016/j.micron.2015.04.003

15. M. Shabaninejad, J. Middleton, S. Latham et al., Pore-scale analysis of residual oil in a reservoir sandstone and its dependence on water flood salinity, oil composition and local mineralogy. Energy Fuel. **31**, 13221–13232 (2017). https://doi.org/10.1021/acs.energyfuels.7b01978

16. K.L. Xi, Y.C. Cao, K.Y. Liu et al., Authigenic minerals related to wettability and their impacts on oil accumulation in tight sandstone reservoirs: an example from the Lower Cretaceous Quantou Formation in the southern Songliao Basin, China. J. Asian. Earth. Sci. **178**, 173–192 (2018). https://doi.org/10.1016/j.jas.2010.03.005

17. L. Ganzer, S. Schatzmann, C.D. Sattler et al., Evaluation of digital rock methodology to complement rock laboratory experiments. Oil. Gas Euro. Mag. **39**, 43–47 (2013)

18. L. Wang, Y.M. He, X. Peng et al., Pore structure characteristics of an ultradeep carbonate gas reservoir and their efffects on gas storage and percolation capacities in the Deng IV member, Gaoshiti-Moxi Area, Sichuan Basin, SW China. Mar. Petrol. Geol. **111**, 44–65 (2020). https://doi.org/10.1016/j.marpetgeo.2019.08.012

19. X.J. Liu, H.L. Zhu, L.X. Liang, Digital rock physics of sandstone based on micro-CT technology. Chin. J. Geophys. **57**, 1133–1140 (2014). https://doi.org/10.6038/cjg20140411

20. B. Bai, R. Zhu, S. Wu et al., Multi-scale method of nano (Micro)-CT study on microscopic pore structure of tight sandstone of Yanchang Formation, Ordos Basin. Petrol. Explor. Dev. **40**, 354–358 (2013). https://doi.org/10.1016/s1876-3804(13)60042-7

21. S.W. Zhou, G. Yan, H.Q. Xue et al., 2D and 3D nanopore characterization of gas shale in Longmaxi formation based on FIB-SEM. Mar. Petrol. Geol. **73**, 174–180 (2016). https://doi.org/10.1016/j.marpetgeo.2016.02.033

22. Z. Zhao, X.P. Zhou, An integrated method for 3D reconstruction model of porous geomaterials through 2D CT images. Comput. Geosci. (2018). https://doi.org/10.1016/j.cageo.2018.11.012

23. C.Y. Lin, Q.Y. Wu, L.H. Ren et al., Review of digital core modeling methods. Prog. Geophys. **33**, 679–689 (2018). https://doi.org/10.6038/pg2018BB0335 (**in Chinese**)

24. T.F. Faisal, A. Islam, M.S. Jouini et al., Numerical prediction of carbonate elastic properties based on multi-scale imaging. Geomech. Energy Environ. **20**, 1–15 (2019). https://doi.org/10.1016/j.gete.2019.100125

25. Z. Zhao, X.P. Zhou, Digital microstructure insights to phase evolution and thermal flow properties of hydrates by X-ray computed tomography. Sci. China Technol. Sci. (2020). https://doi.org/10.1007/s11431-020-1579-x

26. S.Y. An, J. Yao, Y.F. Yang et al., Influence of pore structure parameters on flow characteristics based on a digital rock and the pore network model. J Nat. Gas. Sci. Eng. **31**, 156–163 (2016). https://doi.org/10.1016/j.jngse.2016.03.009

27. L. Zhang, W.L. Jing, Y.F. Yang et al., The Investigation of permeability calculation using digital core simulation technology. Energies **12**, 3273 (2019). https://doi.org/10.3390/en12173273

28. J.J. Li, Y. Liu, Y.J. Gao et al., Pore-scale study of the pressure-sensitive effect of sandstone and its influence on multiphase flows. Petrol. Sci. **16**, 382–395 (2019). https://doi.org/10.1007/s12182-018-0266-6

29. J. Lei, B.Z. Pan, L.H. Zhang, Advance of microscopic flow simulation based on digital cores and pore network. Prog. Geophys. **33**, 653–660 (2018). https://doi.org/10.6038/pg2018BB0108 (**in Chinese**)

30. M.S. Jouini, S. Vega, A. Al-Ratrout, Numerical estimation of carbonate rock properties using multiscale images. Geophys. Prospect. **63**, 405–421 (2015). https://doi.org/10.1111/1365-2478.12156

31. M.J. Blunt, B. Bijeljic, H. Dong et al., Pore-scale imaging and modelling. Adv. Water. Resour. **51**, 197–216 (2013). https://doi.org/10.1016/j.advwatres.2012.03.003

32. Z. Zhao, X.P. Zhou, Establishment of numerical cracking constitutive models using 3D reconstruction and X-ray CT images of geomaterials. Int. J. Mech. Sci. **183**, 105814 (2020). https://doi.org/10.1016/j.ijmecsci.2020.105814

33. J.E. Elkhoury, R. Shankar, T.S. Ramakrishnan, Resolution and limitations of X-ray micro-CT with applications to sandstones and limestones. Transp. Porous. Med. **129**, 413–425 (2019). https://doi.org/10.1007/s11242-019-01275-1

34. R.S. Devarapalli, A. Islam, T.F. Faisal et al., Micro-CT and FIB–SEM imaging and pore structure characterization of dolomite rock at multiple scales. Arab. J. Geosci. **10**, 360–372 (2017). https://doi.org/10.1007/s12517-017-3120-z

35. S. Latham, T. Varslot, A. Sheppard, Image registration: enhancing and calibrating X-ray micro-CT imaging. Imaging Soc. Core Anal. Pap. **2008**, 1–12 (2008)

36. Ø. Markussen, H. Dypvik, E. Hammer et al., 3D characterization of porosity and authigenic cementation in Triassic conglomerates/arenites in the Edvard Grieg field using 3D micro-CT imaging. Mar. Petrol. Geol. **99**, 265–281 (2019). https://doi.org/10.1016/j.marpetgeo.2018.10.015

37. G. Desbois, J.L. Urai, P.A. Kukla et al., High-resolution 3D fabric and porosity model in a tight gas sandstone reservoir: a new approach to investigate microstructures from mm- to nm-scale combining argon beam cross-sectioning and SEM imaging. J. Petrol. Sci. Eng. **78**, 243–257 (2011). https://doi.org/10.1016/j.petrol.2011.06.004

38. H. Izadi, M. Baniassadi, F. Hormozzade et al., Effect of 2D image resolution on 3D stochastic reconstruction and developing petrophysical trend. Transp. Porous. Med. **125**, 41–58 (2018). https://doi.org/10.1007/s11242-018-0997-2

39. X.F. Liu, J.F. Wang, L. Ge et al., Pore-scale characterization of tight sandstone in Yanchang Formation Ordos Basin China using micro-CT and SEM imaging from nm- to cm-scale. Fuel **209**, 254–264 (2017). https://doi.org/10.1016/j.fuel.2017.07.068

40. W. Lin, X.Z. Li, Z.M. Yang et al., Construction of dual pore 3-D digital cores with a hybrid method combined with physical experiment method and numerical reconstruction method. Transp. Porous. Med. **120**, 227–238 (2017). https://doi.org/10.1007/s11242-017-0917-x

41. C. Tian, L.C. Jia, S. Li et al., Petrology characteristics of uranium-bearing sandstone in the southern Ordos basin. U. Geol. **2**, 71–76 (2007) (**in Chinese**)

42. S. Zeng, K.X. Tan, X.M. Du et al., The effects of structural characteristics of low seepage sandstone uranium ore rock on permeability. Adv. Mater. **524–527**, 371–374 (2012)

43. H. Li, H. Zhou, Progress and prospect of research on solute transport during in-situ leaching of uranium. Chin. J. Rare Met. **43**, 319–330 (2019). https://doi.org/10.13373/j.cnki.cjrm.XY18120015

44. C. Tang, X.Z. Sima, Q. Zhu et al., Carbon and oxygen isotopic composition and uranium mineralization significance of calcite of Zhiluo Formation uranium-bearing sandstones in Dongsheng area. Geol. J. China Univ. **22**, 698–706 (2016). https://doi.org/10.16108/j.issn1006-7493.2016055 (**in Chinese**)

45. G.W. Huang, F.C. Yu, J.Y. Pan et al., Geochemical characteristics of trace elements and sulfur isotopes of pyrite from Mengqiguer uranium deposit, Xinjiang: Implication for uranium mineralization. Geo. China **2019**, 1–16 (2019) (**in Chinese**)

46. X.X. Kong, D.S. Xiao, S. Jiang et al., Application of the combination of high-pressure mercury injection and nuclear magnetic resonance to the classification and evaluation of tight sandstone reservoirs: a case study of the Linxing Block in the Ordos Basin. Nat. Gas. Ind. **40**, 38–47 (2020). https://doi.org/10.3787/j.issn.1000-0976.2020.03.005 (**in Chinese**)

47. G. Wang, X.J. Qin, J.N. Shen et al., Quantitative analysis of microscopic structure and gas seepage characteristics of low-rank coal based on CT three-dimensional reconstruction of CT images and fractal theory. Fuel **256**, 1–11 (2019). https://doi.org/10.1016/.fuel.2019.115900

48. H.W. Zhou, J.C. Zhong, W.G. Ren et al., Characterization of pore fracture networks and their evolution at various measurement scales in coal samples using X-ray μCT and a fractal method. Int. J. Coal. Geol. **189**, 35–49 (2018). https://doi.org/10.1016/j.coal.2018.02.007

49. J. Lai, G. Wang, Z. Wang et al., A review on pore structure characterization in tight sandstones. Earth Sci. Rev. **177**, 436–457 (2018). https://doi.org/10.1016/j.earscirev.2017.12.003

50. P.H. Nelson, Pore-throat sizes in sandstones, tight sandstones, and shales. AAPG Bull. **93**(3), 329–340 (2009). https://doi.org/10.1306/10240808059

51. Avizo, Avizo software users guide (2019). https://www.fei.com/software/avizo-user-guide.

52. F.L. Bookstein, Size and shape spaces for landmark data in two dimensions. Stat. Sci. **1**, 181–222 (1986). https://doi.org/10.1214/ss/1177013696

53. L.C. Cui, J.M. Sun, W.C. Yan et al., Construction of multi-scale and-component digital cores based on fusion of different resolution core images. J. Jilin Univ. Earth Sci. Ed. **47**, 1904–1912 (2017) (**in Chinese**)

54. S.J. Redmond, C. Heneghan, A method for initialising the K-means clustering algorithm using kd-trees. Pattern. Recogn. Lett. **28**, 965–973 (2007). https://doi.org/10.1016/j.patrec.2007.01.001

55. Y.W. Gao, W. Wu, Q. Zhang et al., CT image segmentation using multi-Otsu thresholding algorithm and scanning electron microscopy. J. Yangtze. Univ. Nat. Sci. Ed. **16**, 17–24 (2019). https://doi.org/10.16772/j.cnki.1673-1409.2019.04.003 (**in Chinese**)

56. C. Chen, S.H. Lu, J.Q. Li et al., Digital core modeling construction of different lithofacies shale: a case study of Dongying depression. Geoscience **31**, 1069–1078 (2017). https://doi.org/10.3969/j.issn.1000-8527.2017.05.016 (**in Chinese**)

57. X.P. Zhou, Y.X. Zhang, Q.L. Ha, Real-time computerized tomography (CT) experiments on limestone damage evolution during unloading. Theor. Appl. Fract. Mech. **50**, 49–56 (2008). https://doi.org/10.1016/j.tafmec.2008.04.005

58. Z. Zhao, X.P. Zhou, Pore-scale effect on the hydrate variation and flow behaviors in microstructures using X-ray CT imaging. J. Hydrol. **584**, 124678 (2020). https://doi.org/10.1016/j.jhydrol.2020.124678

59. Z. Zhao, X.P. Zhou, Digital measurement of 2D and 3D cracks in sandstones through improved pseudo color image enhancement and 3D reconstruction method. Int. J. Numer. Met. **43**, 2565–2584 (2019). https://doi.org/10.1002/nag.2993

60. J.J. Wang, Q.J. Kang, Y.Z. Wang et al., Simulation of gas flow in micro-porous media with the regularized Lattice Boltzmann method. Fuel **205**, 232–246 (2017). https://doi.org/10.1016/j.fuel.2017.05.080

61. Z. Zhao, X.P. Zhou, Q.H. Qian, Fracture characterization and permeability prediction by pore scale variables extracted from X-ray CT images of porous geomaterials. Sci. China Technol.

Sci. **63**, 755–767 (2020). https://doi.org/10.1007/s11431-019-1449-4

62. X.P. Zhou, Z. Zhao, Z. Li, Cracking behaviors and hydraulic properties evaluation based on fractural microstructure models in geomaterials. Int. J. Rock. Mech. Min. Sci. **130**, 104304 (2020). https://doi.org/10.1016/j.ijrmms.2020.104304

63. H.M. Dong, J.M. Sun, Z.Z. Lin et al., Quantitative characterization and characteristics analysis of microscopic pore structure in natural gas hydrate based on CT scanning. J. China Un. Petrol. Nat. Sci. **42**, 40–49 (2018). https://doi.org/10.3969/j.issn.1673-5005.2018.06.005 (**in Chinese**)

64. D. Zheng, Z. Reza, Pore-network extraction algorithm for shale accounting for geometry-effect. J. Petrol. Sci. Eng. **176**, 74–84 (2019). https://doi.org/10.1016/j.petrol.2019.01.046